Composition regulation of composite materials in laser powder bed fusion additive manufacturing

Yao, Dengzhi; Wang, Ju ; Cai, Yao ; Zhao, Tingting ; An, Xizhong; Zhang, Hao; Fu, Haitao ; Yang, Xiaohong ; Zou, Qingchuan ; Wang, Lin

Important note
To cite this publication, please use the final published version (if applicable).
Please check the document version above.

Contents lists available at ScienceDirect

Powder Technology

Composition regulation of composite materials in laser powder bed fusion additive manufacturing

Dengzhi Yao [a], Ju Wang [a], Yao Cai [a], Tingting Zhao [b], Xizhong An [a,*], Hao Zhang [a], Haitao Fu [a], Xiaohong Yang [a], Qingchuan Zou [a], Lin Wang [c]

[a] Key Laboratory for Ecological Metallurgy of Multimetallic Mineral of Ministry of Education, School of Metallurgy, Northeastern University, Shenyang 110819, Liaoning, PR China
[b] Key Laboratory of Solidification Control and Digital Preparation Technology, School of Materials Science and Engineering, Dalian University of Technology, Dalian 116024, China
[c] Resource & recycling, Department of Engineering Structures, Faculty of Civil Engineering and Geosciences, Delft University of Technology, Stevinweg 1, 2628 CN Delft, the Netherlands

HIGHLIGHTS

- The spreading of binary WC/316L composite powders was numerically investigated.
- The parametric studies on segregation behavior were systematically conducted.
- The underlying mechanisms were identified from microscopic scale.
- Composition control of composite materials was realized by regulating segregation.

GRAPHICAL ABSTRACT
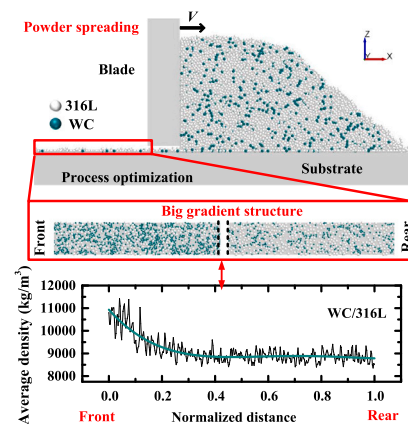
ARTICLE INFO

ABSTRACT

Understanding and controlling the composition segregation during powder spreading is of key importance in the additive manufacturing (AM) of composite materials. Under this circumstance, the segregation behavior of WC/316 L composite powders during spreading in laser powder bed fusion (LPBF) AM was numerically investigated by the discrete element method. The effects of process conditions (i.e., spreader velocity and geometry) and powder properties (i.e., size and shape of the WC powder) on the powder bed composition segregation and related characteristics were systematically analyzed. Corresponding mechanisms were identified from microscopic scale in terms of particle velocity, motion trajectory, mechanical behavior, and energy information. Finally, proper solutions in designing and constructing WC/316 L composite materials with desired gradient structures were proposed. The results show that the small blade velocity (V) will enhance the negative

* Corresponding author.
  E-mail address: anxz@mail.neu.edu.cn (X. An).

segregation, increase the average packing density $\bar{\rho}$, and decrease uniformity ρ_{vc} in the WC/316 L composite powder bed. Compared with the blade, the roller can increase the negative segregation ($Se_{roller} = -0.027 < Se_{blade} = -0.019$) and the average packing density ($\bar{\rho}_{roller} = 0.31 > \bar{\rho}_{blade} = 0.20$). When the WC/316 L size ratio increases from 25 μm/45 μm to 45 μm/45 μm, the negative segregation becomes weaker, and its value increases from -0.084 to -0.007. When the size ratio increases to 65 μm/45 μm, the powder behaves positive segregation with $Se_{max} = 0.017$; in this case, the packing density is the lowest (0.14), and the uniformity is the worst (0.17). In comparison with spherical shape, polyhedral WC powder can reduce the negative segregation of the powder bed ($Se_{sphere} = -0.019 < Se_{polyhedron} = -0.008$), while the WC shape has less effect on the packing density and uniformity. The density difference of the WC and 316 L powders leads to the difference in energy and force, resulting in different motion and segregation behaviors in the composite powder bed. For WC/316 L composite powder with a fixed composition, the condition of $V = 0.025$ m/s, WC/316 L size ratio = 25 μm/45 μm, roller spreader, and spherical WC can realize the proper composition gradient along the spreading direction in the composite powder bed.

1. Introduction

Metal materials play an important role in the history of human development due to their marvelous properties. However, the requirements for the comprehensive performance of materials become more prominent with the development of industrial technology, and the elemental metal material seems unlikely to satisfy the increasingly severe challenges [1–3]. Incorporating reinforced phase particles (e.g., oxides, intermetallics, nitrides, carbides, and borides, etc.) into the metal matrix can create new particulate reinforced metal matrix composite (PRMMC) [4,5], which can benefit from the properties of both reinforced particles and metal matrix, so that the materials not only have high strength, high toughness, and good thermal conductivity of the metal matrix, but also possess high hardness, long fatigue life, and high wear resistance of the reinforced particles [6]. Therefore, this type of material has been widely used in aerospace, automobile manufacturing, and national defense [7,8], etc.

Traditional manufacturing methods of PRMMCs mainly include casting [9–11] and powder metallurgy [12]. However, these approaches have the disadvantages of high manufacturing costs and the inability to produce parts with high precision and complex structures. In comparison, additive manufacturing (AM) is an ideal alternative for fabricating PRMMCs due to its high flexibility, free for structure complexity, and low material waste [13,14], which has attracted more and more research interests in recent years. According to the composition distribution, the PRMMCs can be simply divided into homogeneous composites (materials with uniform composition) and heterogeneous composites (materials with gradient composition). In general, homogeneous composites can be produced by selective laser melting [6,15,16], laser cladding [17,18], and laser direct deposition technology [19]. It can be found that the preparation of homogeneous composite materials has been relatively mature in various AM fields, including powder bed-based AM or energy direct deposition technology. While the gradient composites can only be prepared by energy direct deposition techniques [20–25], which is mainly due to the unique powder supply mode, that is, different composition gradients are obtained by replacing different powders. Nonetheless, in fabricating gradient composites by energy direct deposition techniques, disadvantages like higher surface roughness, lower accuracy, and lower powder recyclability compared to laser powder bed fusion (LPBF) [26,27] are obvious. In this case, can the desired gradient composition of composite powders be realized by powder bed-based additive manufacturing? How to achieve composition control of composites by parametric regulation? With these questions, the spreading of WC/316 L composite powders in LPBF AM will be investigated to find corresponding answers.

LPBF is a popular powder bed-based AM technology with the features of high flexibility, no mold, and structural constraints, which has been widely used in many key industrial areas [28–30]. As the first step, the powder spreading can significantly affect the quality and performance of the final AM products [31,32]. In our previous work, particle size segregation occurs during the powder spreading process [33], that

is, the small particles are easier to deposit in the early stage than big ones [34–36]. However, compared with particle size, density difference is also the main factor causing segregation [37]. Current problems yet to be solved include: (1) Will segregation occur when two powders with different densities are spread and can it cause composition gradient along the spreading direction? (2) What factors can affect composition segregation? (3) Can different gradient composites be obtained by regulating component segregation? (4) And how?

In this paper, the spreading of binary WC/316 L stainless steel composite powders during LPBF AM process was numerically reproduced by discrete element method (DEM). The effects of process parameters and powder properties on segregation behavior and related macroscopic characteristics (packing density and uniformity) of the composite powder beds were systematically studied. And the underlying segregation mechanisms were analyzed from microscopic scale in terms of particle velocity, motion trajectory, mechanical behavior, and energy information. Finally, proper solutions for constructing desired gradient structure of WC/316 L composites were proposed. It is hoped that the obtained highlighted results can provide new insights for the design and fabrication of composite materials with controlled composition distributions and structures.

2. Methods

2.1. Discrete element method

In DEM model, the translational motion and rotational motion of each particle are governed by Newton's second law [38,39]:

$$m_i \frac{dv_i}{dt} = \sum_{j=1}^{p} \left(F_{ij,n} + F_{ij,s} \right) + m_i g \tag{1}$$

$$I_i \frac{d\omega_i}{dt} = \sum_{j}^{p} \left(T_{ij,s} + T_{ij,r} \right) \tag{2}$$

where m_i, v_i, ω_i and I_i are the mass, translational velocity, angular velocity, and movement of inertia, respectively; $F_{ij,n}$ and $F_{ij,s}$ represent the normal contact force and tangential contact force between particles i and j. The torque $T_{ij,s}$ is generated by the tangential force, and the torque $T_{ij,r}$ is generated by the rolling friction. The elastic contact forces are described by Hertz-Mindlin contact model, and the cohesive forces between particles are accounted by the JKR model [40,41]. The normal contact force between particles can be expressed by:

$$F_{ij,n} = \frac{4E^*}{3R^*} r^3 - 4\sqrt{\pi r^3 \gamma E^*} \tag{3}$$

where γ, E^* and R^* are surface energy, equivalent Young's modulus and equivalent contact radius, respectively. The contact radius r in Eq. (3) can be determined by the normal overlap α. More details on the equations utilized in DEM simulation have been summarized in Table A1 in
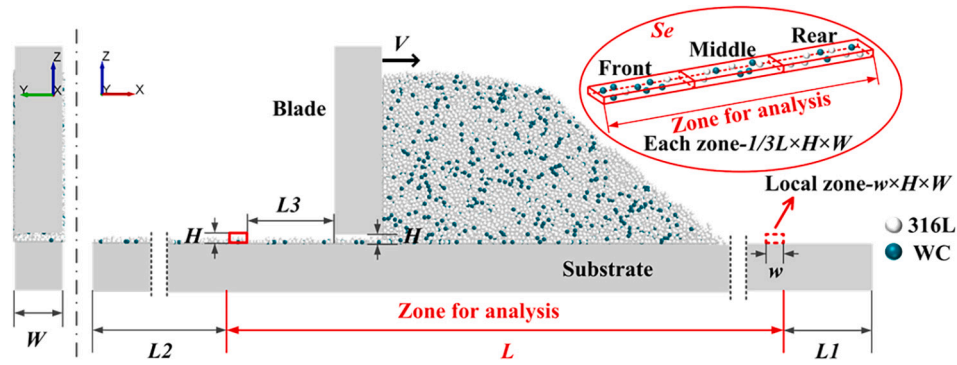
Fig. 1. Snapshot of powder spreading.

Table 1
Parameters used in the simulations.

Parameters	Base value
L, mm	37.7
$L1$, mm	2
$L2$, mm	10.3
$L3$, mm	2
W, mm	0.05
w, mm	0.02
Gap height H, μm	100

Table 2
Physical parameters of the WC powder.

Parameters	Base value
Poisson's ratio ξ, −	0.3
Theoretical density ρ, kg/m^3	15,630
Young's modulus E, Pa	2.2×10^8
Coefficient of restitution e, −	0.64
Coefficient of sliding friction μ_s, −	0.6
Coefficient of rolling friction μ_r, −	0.085
Surface energy γ, J/m^2	0.001

the Appendix.

$$\alpha = r^2/R^* - \sqrt{\frac{2\pi\gamma r}{E^*}} \tag{4}$$

2.2. Simulation conditions

In the simulations, WC (20 wt%)/316 L composite powders were selected for research [6]. For more accurately realizing the composition control, mono-sized WC powder and 316 L powder, which have been employed in actual additive manufacturing [19,42], were numerically investigated. A rectangular computational domain with dimensions (X-Y-Z) of 50 mm × 0.5 mm × 5 mm was chosen for analysis. And symmetrical boundary conditions were applied in the Y direction of the computational domain. One snapshot of spreading and corresponding parameters are shown and listed in Fig. 1 and Table 1, respectively. The spreading velocity is 0.05 m/s when studying the effect of WC/316 L size ratios [36], while the velocity is 0.025 m/s when investigating the influences of spreader geometry and WC particle shape. Relevant reasons will be given in Section 3.2. The physical parameters of 316 L stainless steel powder have been systematically verified in the previous study [43], while those for the WC powder were given in Table 2 by considering the 316 L powder [44].

In the present work, the surface of the substrate is set to be flat. Before spreading, the two powder particles are randomly generated under gravity in a zone with dimension (X-Y-Z) of 3 mm × 0.5 mm × 4.7 mm to form an initial powder pile. Then the composite powder pile moves forward under the action of the spreader. In this duration, the particles continuously flow through the gap between the spreader and substrate to form a powder bed. It needs to mention that the local zone (i.e., data collection zone) moves along the spreading direction with the spreader, collecting data at regular intervals. The utilized time interval under different spreading velocities (V = 0.025, 0.05, 0.075, 0.1 m/s) are 0.004 s, 0.002 s, 0.001333 s, and 0.001 s, respectively. The collected data are all from the particles inside the cuboid. The different metrics (packing density, average apparent density, and composition) in Section 3 are all derived from this process. Note that the base size (diameter) of 316 L/WC powder is set as 45 μm/45 μm in the study. Here, the base size of 316 L powder is derived from the practical 3D printing powder purchased from Shenyang Institute of Rare Metals [33,43]. The base size of WC powder is also set according to that of 316 L stainless steel powder. The size range of WC powder below is derived from others' work [19,45–47].

3. Results and discussion

3.1. Packing density and uniformity

As an important indicator of the macroscopic characteristics, powder bed packing density (ρ) and uniformity (ρ_{vc}) can seriously affect the molten layer quality [38,41]. In this section, the influences of process parameters and powder properties on the macroscopic characteristics of composite powder beds are systematically investigated, where ρ and ρ_{vc} are calculated by:

$$\rho = \frac{V_p}{V_c} \tag{5}$$

$$\rho_{vc} = \frac{\rho_{st}}{\overline{\rho}} \tag{6}$$

where: V_p and V_c represent the volumes of the powder and the container, respectively; ρ_{st} is the standard deviation of packing densities; $\overline{\rho}$ is the average packing density. Lower ρ and larger ρ_{vc} indicate much looser structure and more inferior uniformity of the powder bed. Fig. 2 shows the effects of process parameters and powder properties on the evolutions of packing density, average packing density and uniformity of WC/316 L composite powders, where the packing density distributions in the powder beds obtained under different blade velocities V are firstly investigated as depicted in Fig. 2(a). One can find that the impact of V on
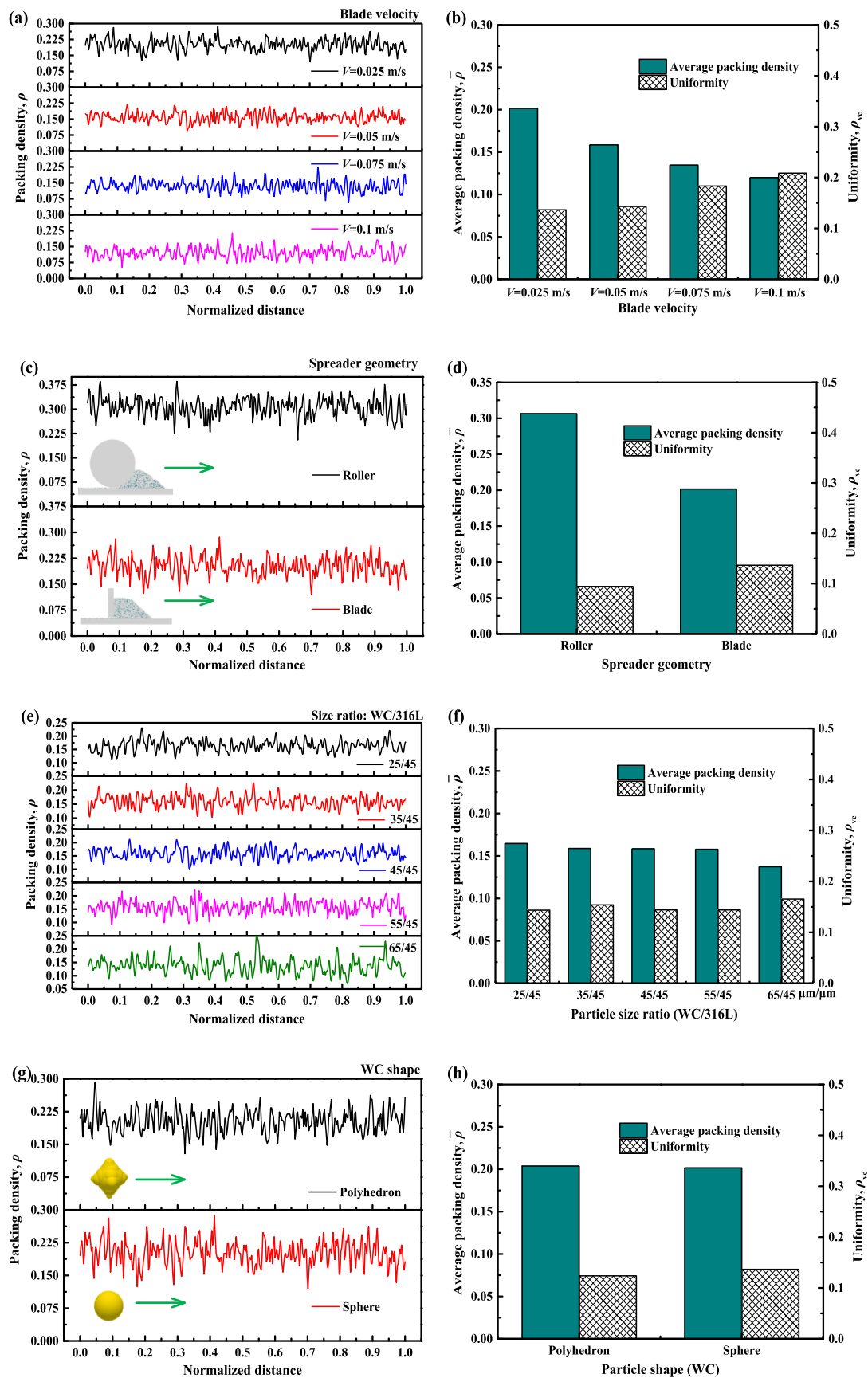
Fig. 2. Evolutions of packing density, average packing density, and uniformity of composite powder beds under different conditions, where: (a, b) different blade velocities; (c, d) different spreader geometries; (e, f) different WC/316 L particle size ratios; (g, h) different WC shapes.
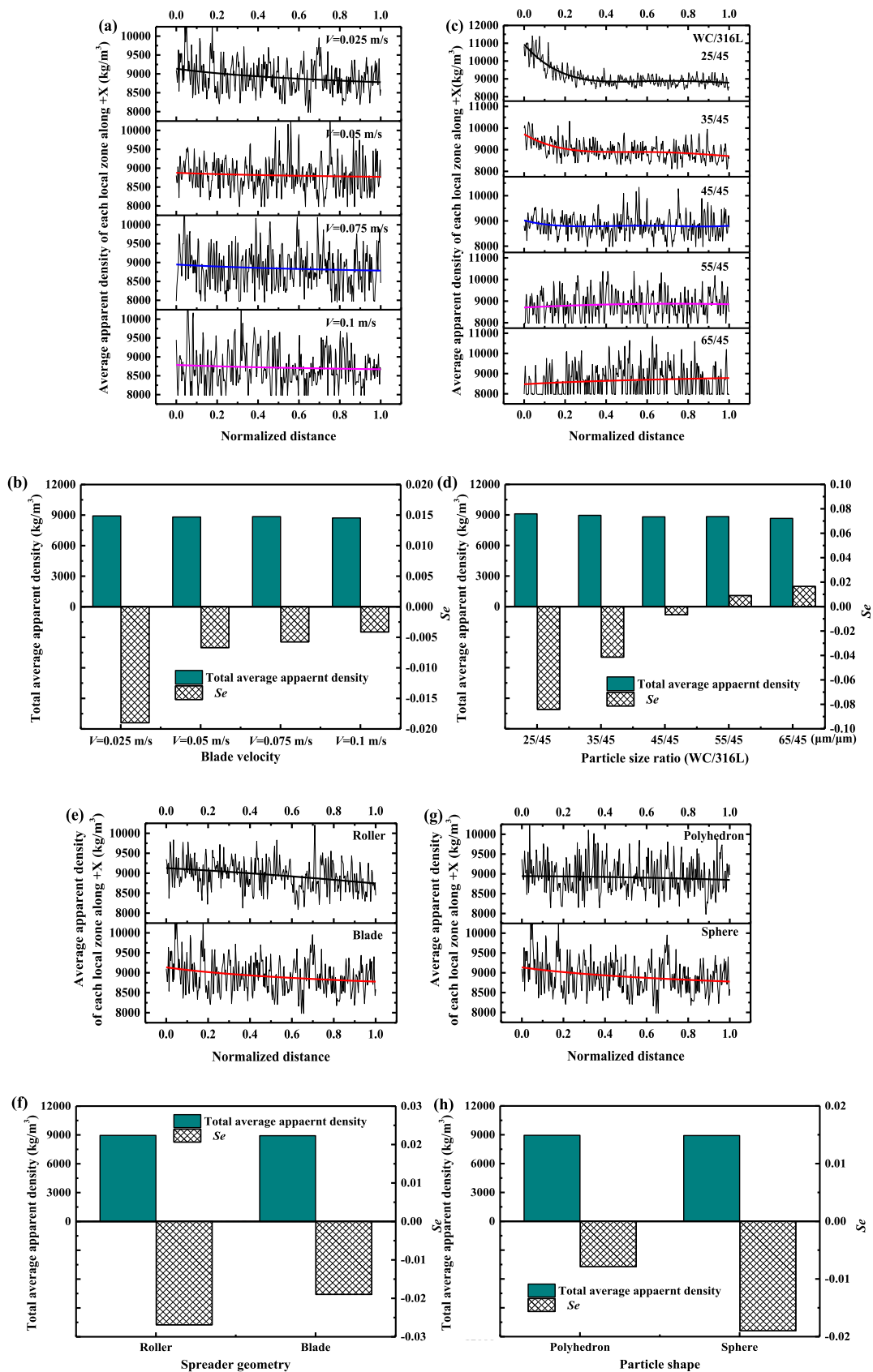
Fig. 3. Average apparent density evolutions and corresponding total average densities and segregation degrees for composite powder beds formed under different conditions, where: (a, b) different blade velocities; (c, d) different WC/316 L powder size ratios; (e, f) different spreader geometries; (g, h) different WC particle shapes.

ρ of the composite powder beds is basically similar to that of the elemental powder [38]. When $V = 0.05$ m/s, the packing density of the powder bed fluctuates around the average value. The larger the blade velocity, the lower the packing density of the spread composite powder bed. This is mainly due to the high instability of powder flow induced by the high blade velocity [48]. This conclusion can be confirmed by the average packing density evolution in Fig. 2(b). As can be observed that the average packing density of the composite powder bed decreases from 0.2 to 0.12 when the blade velocity increases from 0.025 m/s to 0.1 m/s; also, the uniformity increases from 0.14 to 0.21, implying that large V can reduce the powder bed uniformity. This can also be ascribed to the instability induced by the high blade velocity [48].

The effects of spreader geometry (roller and blade) on the evolution of macroscopic characteristics of the composite powder beds are illustrated in Figs. 2(c) and (d). It should be noted that the radius of the roller is 2 mm, which moves along the X direction (from left to right) with a constant translational velocity (0.025 m/s) and rotates anti-clockwise with a constant angular velocity (60 rad/s) [40]. As can be seen that the spreader geometries greatly affect the packing density of the powder bed. The average packing density of the composite powder bed formed by the roller is 0.31, which is much larger than 0.20 formed by the blade. This is mainly due to the extrusion behavior from the roller when the powder flows into the gap [32,36,49]. In addition, the uniformity of the powder bed formed by the roller is 0.094, lower than 0.137 by the blade, demonstrating that the roller can improve the uniformity of the powder bed. On the other hand, the counterclockwise rotation of the roller breaks the strong force arches in the powder pile in front of the spreader, which makes the powder flow more smoothly [35,50]. Together with the special compression from the rotating roller, the spread powder bed becomes more uniform.

Evolutions of packing density, average packing density, and uniformity of composite powder beds under various WC/316 L size ratios are shown in Figs. 2(e) and (f), respectively. It should be emphasized that the size of 316 L powder is fixed to be 45 μm, only the size of WC powders is changed in the range of 25–65 μm. As illustrated, the influence of the WC particle size on the packing density of the composite powder bed is not significant. This is mainly due to the small content of the WC powder. Only with large size difference between the two powders (e.g., WC/316 L = 65 μm/45 μm), the packing density of the powder bed is notably small with a minimum value of 0.14. Besides, it can also be found that with WC/316 L = 65 μm/45 μm, the powder bed uniformity becomes worse with the largest ρ_{vc} value of 0.17. The low packing density and poor uniformity can be ascribed to the fluctuation of the powder flow caused by the large sized particles [51].

In real production, two shaped WC powders, i.e., polyhedron and sphere [15,18,52], are commonly used. In this section, the equal sized regular octahedral WC powder with sharp-edged profile is chosen for study. It should be noted that the sphere assembly model is utilized to construct the octahedral WC particles [53,54]. Although this method does not really reflect the sharp-edged profiles, the generated powder can still reflect the weak flowability of complex polyhedral WC to some extent compared with the spherical powder. Here, each octahedral WC particle is composed of 28 element-spheres. Figs. 2(g) and (h) illustrated the evolutions of packing density, average packing density and uniformity of composite powder beds including different shaped WC particles. The inset figures provide the morphologies of the utilized two WC particle shapes, where the octahedron shape is formed equivalently from spherical particles of the same volume. Similarly, for the two WC powders involved, no obvious difference in the evolution of these macroscopic characteristics can be observed, implying that a small amount of polyhedral reinforced particles is not likely to create significant effects on the packing properties of the composite powder bed.

3.2. Effects of process parameters and powder properties

In addition to the macroscopic characteristics, the uniformity of the microscopic composition of the powder bed is also of key importance. In this section, the distribution state of the two powders in the composite powder bed, which is inextricably linked to the structural fabrication of composites, is quantitatively reflected by the average apparent density:

$$\text{Average apparent density} = \frac{m_{\text{WC}} + m_{\text{316L}}}{v_{\text{WC}} + v_{\text{316L}}} \quad (7)$$

where m_{WC} and m_{316L} are the masses of WC and 316 L powders in the measurement zone (local zone in Fig. 1), and v_{WC} and v_{316L} mean the volumes of the two powders. In this article, the maximum average apparent density is 15,630 kg/m^3, indicating that this region is filled with WC powder. And the minimum average apparent density is 7980 kg/m^3, implying that this region is filled only by 316 L powder. The larger the average apparent density, the higher the content of WC. It should be emphasized that the average apparent density of the initial WC (20 wt%)/316 L composite powders is 8846 kg/m^3 calculated by the above equation.

Fig. 3(a) depicts the average apparent density evolution of each local zone along +X for composite powders with different blade velocities. One can find that the average apparent density of the powder bed under each condition fluctuates around its average. The difference is that under the small spreading velocity (e.g., $V = 0.025$ m/s), the average apparent density in the front region of the composite powder bed is obviously higher, and that in the rear is lower. There is a decreasing trend from left to right, meaning that the content of WC in the front of the powder bed is higher and that in the rear is lower. The distribution of WC is not uniform, indicating the occurrence of component segregation of WC in the composite powder bed.

To intuitively evaluate the composition segregation in the composite powder bed, the segregation degree (*Se*) is introduced [33]. Here, the analysis zone (marked in Fig. 1) is equally divided into three sections, where the specific locations and sizes are clearly indicated. X_{Front} and X_{Rear} of the front and rear regions are utilized to calculate *Se*:

$$Se = \frac{X_{\text{Rear}} - X_{\text{Front}}}{\overline{X}} \quad (8)$$

where the values of X_{Front} and X_{Rear} are the average of X in the front and rear regions. $\overline{X}$ is the average of the whole powder bed. It is noted that X represents apparent density in Section 3.2 and mass fraction of the two powders in Section 3.3. *Se* can reflect the segregation degree in the powder bed. $Se = 0$ or $Se \approx 0$ means no segregation. Positive segregation (+*Se*) occurs in the powder bed when $Se > 0$, i.e., the value of X in the front region is lower than that in the rear region. Negative segregation (—*Se*) occurs in the powder bed when $Se < 0$, which is opposite to positive segregation.

Fig. 3(b) illustrates the total average apparent density and segregation degree with different blade velocities. One can find that all values of total average apparent densities under different blade velocities are similar, indicating that blade velocities do not change the composition content of the composite powder bed. The *Se* in Fig. 3(b) shows that the segregation degrees of the powder beds at different blade velocities are negative; i.e., negative segregation occurs in the powder beds, implying that the content of WC powder in the front is higher than that in the rear. This is mainly due to the density difference between the two powders, where the reasons will be discussed in Section 3.4. Besides, the smaller the blade velocity, the more serious the negative segregation. When $V = 0.025$ m/s, the *Se* of the powder bed is −0.019; however, when $V = 0.1$ m/s the *Se* of the powder bed is only −0.004, meaning that increasing V
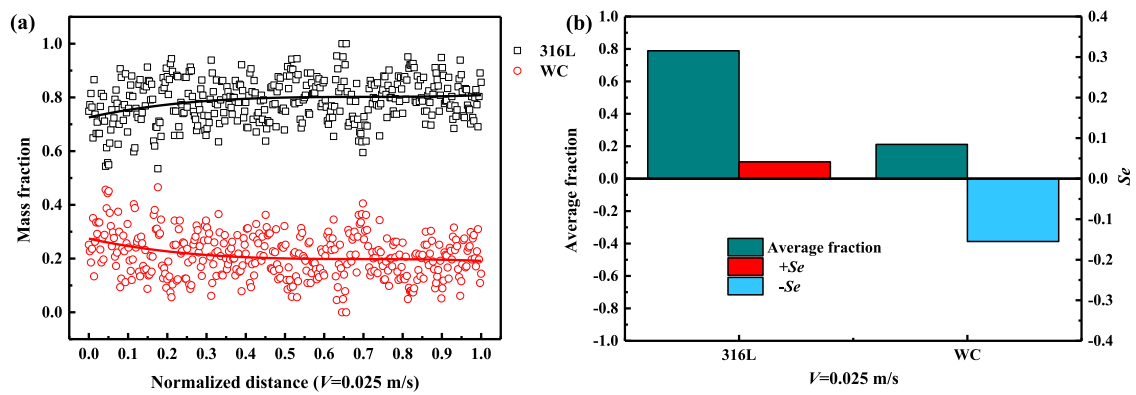
Fig. 4. Under typical condition ($V = 0.025$ m/s), mass fraction evolutions of the two powders (the solid lines are from data fitting) (a) and corresponding average fraction and segregation degree (b).
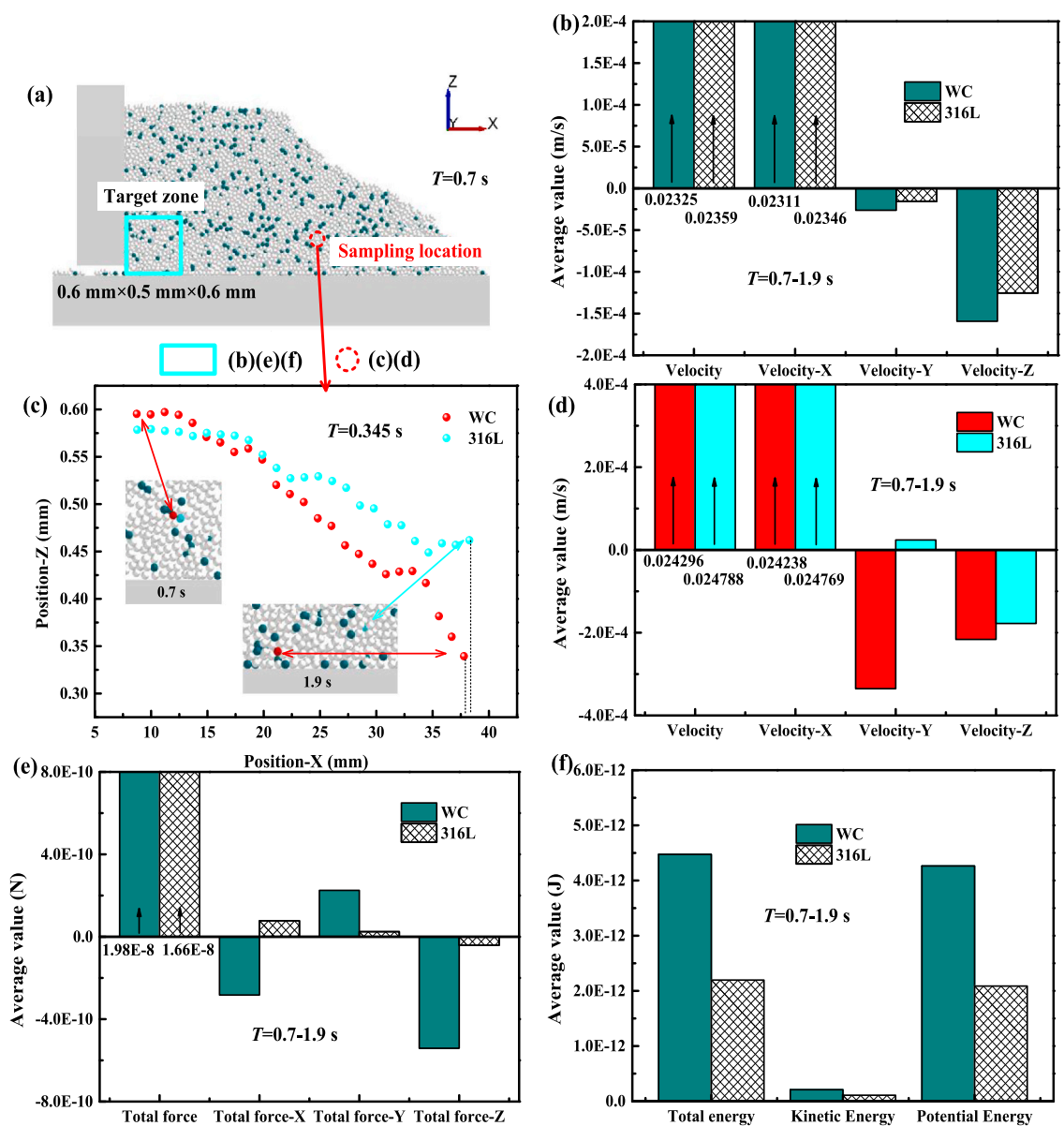
Fig. 5. Macro- and microscopic behaviors of particles, where: (a) morphology of the powder pile; (b) average velocities of the two powders in the blue zone in (a); (c) trajectories of two neighboring particles (WC and 316 L) in the red dotted circles in (a); (d) velocities of the two particles in (c); (e) average forces on the two powders; (e) average energies on the two powders. (For interpretation of the references to colour in this figure legend, the reader is referred to the web version of this article.)

will reduce the time and probability of WC segregation in the composite powder bed [33].

The average apparent density evolutions of the composite powder beds with different WC/316 L size ratios are illustrated in Fig. 3(c). The three subfigures in the upper part (respectively corresponding to WC/316 L = 25 μm/45 μm, 35 μm/45 μm, 45 μm/45 μm) indicate that the larger the size difference between WC and 316 L, the larger difference between the average apparent densities of the front and rear regions; i. e., decreasing the WC powder size increases the segregation behavior, which is helpful for the establishment of gradient composites. From three subfigures in the lower part (WC/316 L = 45 μm/45 μm, 55 μm/45 μm, 65 μm/45 μm), one can find that the large sized WC powder will reduce the negative segregation behavior, which is verified in Fig. 3(d). Clearly, the total average apparent density of the powder bed under different size ratios does not vary significantly. The *Se* as shown in Fig. 3 (d) depicts that negative segregation occurs in the composite powder bed when the size of WC powder is between 25 and 45 μm. As the size decreases from 45 μm to 25 μm, the *Se* decreases from −0.007 to −0.084, indicating that the negative segregation becomes more serious. Positive segregation occurs when the size of WC powder is in the range of 55–65 μm, and the *Se* of the powder bed increases from −0.007 to 0.017 when the size of WC powder changes from 45 μm to 65 μm, implying that increasing the size of WC powder will increase the probability of WC particles depositing at the rear of the powder bed. This is due to the positive size segregation caused by the large sized WC particles. Mechanisms of size segregation can be found in our previous study [33].

From Figs. 3(a) and (b) one can find that a small spreading velocity will amplify the segregation behavior of WC powder during spreading. Therefore, the spreading velocity of 0.025 m/s is employed to investigate the influences of spreader geometries and particle shapes on segregation more accurately. The average apparent density evolutions of composite powder beds obtained by different shaped spreaders are displayed in Fig. 3(e). As can be seen that the average apparent density evolution formed by the roller is basically the same as that formed by the blade. In other words, the average apparent density is high at the front and low at the rear. Fig. 3(f) demonstrates that the *Se* of the composite powder bed is −0.027 when the roller is utilized, which is smaller than that (−0.019) of the blade, meaning that the negative segregation of the roller is significantly greater than that of the blade. This is consistent with the conclusion that the size segregation behavior of the roller is larger than that of the blade [55], which may be ascribed to the complex particle motion and diffusion behavior of the roller system [35]. Under the action of the roller, the particles in the powder pile in front of the spreader have more relative motions [32,49], so that the negative segregation behavior of the roller is much stronger than that of the blade.

Figs. 3(g) and (h) illustrate the average apparent density evolutions and segregation degrees under different WC shapes, respectively. From Fig. 3(g) one can find that the average apparent density evolution of polyhedral WC powder is relatively uniform, while the obvious negative segregation occurs in spherical WC powder. The *Se* of polyhedral WC powder is −0.008, while that of spherical WC is −0.019 as shown in Fig. 3(h), implying that the negative segregation of polyhedral WC powder is smaller than that of spherical WC powder. This is mainly due to the weaker flow and leakage behavior of polyhedral powder than spherical powder [56]. Therefore, the segregation probability of polyhedral powder under the same process condition is relatively small, which can provide references to practical processes by introducing non-spherical WC particles.

3.3. Composition analysis

To further understand the composition segregation of WC/316 L composite powder bed, the mass fraction evolution, average fraction and segregation degree of the two powders when *V* = 0.025 m/s are provided in Fig. 4. From Fig. 4(a) one can find that the mass fraction of WC powder is higher at the front and lower at the rear, that is, the mass fraction of WC is getting smaller from front to rear of the powder bed, which is opposite to the 316 L powder. This can be verified by the segregation degree in Fig. 4(b). Combined with Figs. 3(a) and (b), it is seen that the differences in micro-components lead to the differences in apparent density distribution. Also, the average mass fractions of the two powders in the entire powder bed are similar to the initial set values, approximately 20% (WC) and 80% (316L), indicating that the segregation behavior does not change the overall composition of the composite powder bed, but only alters the uniformity of the components. Evolutions of mass fraction and segregation degree under other conditions are also investigated as plotted in Figs. A1-A4 in the Appendix.

3.4. Segregation mechanism

To comprehensively explore the segregation mechanism in WC/316 L composite powder bed, particle velocity, motion trajectory, mechanical behavior and particle energy of the two powders during spreading are systematically analyzed, as depicted in Fig. 5. It needs to note that the typical case, *V* = 0.025 m/s, is analyzed here. The macroscopic topography of the powder pile during powder spreading is shown in Fig. 5(a). One can find that the positions of WC and 316 L particles in the powder pile are relatively uniform, implying that the segregation is not caused by the uneven initial mixing of the two powders in the powder pile. Firstly, a target zone in front of the blade is selected, and its location is marked in Fig. 5(a). It needs to point out that the target zone is a cuboid that moves with the blade. Secondly, the average values of the total velocity and the sub-velocities in all directions of the two powders in this zone over a period of time (0.7–1.9 s) are analyzed. As illustrated in Fig. 5(b) that the velocity of WC powder in the X direction is lower than that of 316 L powder, while the velocity of WC powder in the Z direction is greater than that of 316 L powder, which will lead to easier deposition and leakage of WC powder onto the substrate. In this case, it is beneficial for the occurrence of segregation.

To more clearly show the motion behavior difference of the two powders, two adjacent particles at the red sampling position in Fig. 5(a) are selected, and their trajectories are plotted in Fig. 5(c). As can be seen that at the initial moment (*T* = 0.7 s), WC and 316 L particles are in contact, and the WC particle is slightly higher than the 316 L particle in Z direction. At *T* = 1.9 s, the moving distance of the WC particle in X direction is slightly smaller than that of the 316 L particle, and the position of the WC particle in the Z direction is evidently lower than that of the 316 L particle. Specifically, the WC particle moves 0.3 mm, while the 316 L particle only moves 0.13 mm in the Z direction. Fig. 5(d) depicts the total velocity and the sub-velocities in all directions of these two particles. As can be seen that during spreading, the average velocity of the WC particle in the X direction is smaller than that of the 316 L particle, while its average velocity in the Z direction is larger, which directly leads to the results in Fig. 5(c).

The difference of particle motion behavior is normally caused by the mechanical behavior and energy information. The average values of the forces on the two powders in the target zone during this period are calculated, as depicted in Fig. 5(e). Clearly, the force on the WC powder in the Z direction is larger than that of the 316 L powder, indicating that the WC powder is prone to flow in the Z direction during the spreading. However, the orientations of the forces on the two powders in the X direction are opposite, implying that the WC powder can be more easily hindered. Therefore, the WC powder is prone to move downward or leak during the spreading process. Besides, for more details, the energy information of the two powders is shown in Fig. 5(f). One can find that the total energy of the two powders is mainly indicated by the potential energy. And the total energy and potential energy contained in the WC powder are larger than those in the 316 L powder. The difference in mechanical behavior and energy information is mainly caused by the difference in density between the reinforced powder (15,630 kg/m^3)
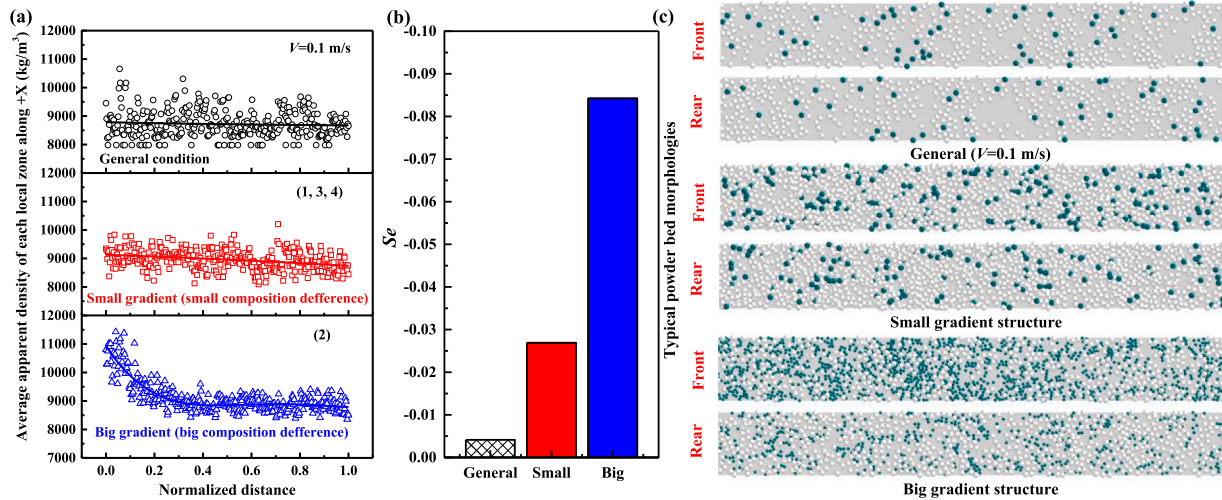
Fig. 6. Comparison of simulation results, where: (a) average apparent density evolutions (the blade velocity of 0.1 m/s, the optimized combination parameters (1, 3, 4) and the optimized condition (2)); (b) segregation degrees; (c) typical morphologies.

and the matrix powder (7980 kg/m^3), which eventually leads to the difference in velocity and the occurrence of segregation.

3.5. Process optimization

Through comprehensive analysis on the aforementioned results, we find that four major conditions should be properly chosen for the design of gradient WC/316 L composite material, which are (1) a small spreading velocity (0.025 m/s); (2) a relatively large size ratio of WC/316 L (e.g., 25 μm/45 μm); (3) roller as the spreader; (4) spherical WC powder. Under this circumstance, the small gradient structure (i.e., the small composition difference) is more likely to be obtained through conditions (1), (3), and (4), while the big gradient structure (i.e., the big composition difference) is prone to be obtained by condition (2). Therefore, we carried out numerical simulations on powder spreading under the optimized conditions of (1, 3, 4) and the optimal condition (2), respectively. The results were compared with those obtained before optimization (when $V = 0.1$ m/s in Fig. 1) as shown in Fig. 6. The evolutions of average apparent densities of the powder beds in Fig. 6(a) indicate that the pronounced apparent density negative segregation occurs in the powder beds using optimal parameters, among which the slight gradient structure can be generated under the combined conditions (1, 3, 4), while the big gradient structure (i.e., the big composition difference) occurs under the optimized condition (2). And the segregation behavior in the powder bed when $V = 0.1$ m/s is weak. Their segregation degrees and macroscopic morphologies are provided in Figs. 6(b) and (c), respectively. From the Se one can find that the obvious gradient structure is established under two optimal conditions, in which the Se of optimized condition (2) is −0.084, while the other one is −0.027. And the conclusion is further confirmed by the macroscopic morphologies. All result comparisons indicate that the gradient structure of the powder bed can be established by changing process parameters and particle properties.

4. Conclusions

In this paper, the discrete element method was utilized to simulate the spreading process of binary WC/316 L composite powders during LPBF additive manufacturing. Firstly, the influences of process

parameters and powder properties on the segregation behavior and related properties of the powder bed were systematically investigated. Then, the dynamic behavior and mechanism of the segregation were analyzed by the microscopic information including particle velocity, motion trajectory, mechanical behavior and particle energy. Finally, proper solutions for constructing desired gradient structure of WC/316 L composites were proposed. The main conclusions are as follows:

1. With other conditions being fixed, when the blade velocity decreases from 0.1 m/s to 0.025 m/s, the average packing density of WC/316 L composite powder bed gradually increases from 0.12 to 0.2, and the uniformity decreases from 0.21 to 0.14. Compared with the blade, the roller can significantly improve the packing density; the uniformity of the two cases is similar. When the WC/316 L size ratio is 65 μm/45 μm, the composite powder bed has the smallest packing density (0.14) and the worst uniformity (0.17). The WC particle shape has less effect on the packing density and uniformity of the composite powder bed.

2. When the blade velocity decreases from 0.1 m/s to 0.025 m/s, the Se of the WC/316 L composite powder bed decreases from −0.004 to −0.019, meaning that the negative segregation becomes more serious. Compared with the blade, the roller increases the negative segregation of WC powder, and its Se reduces from −0.019 to −0.027. When the WC/316 L size ratio increases from 25 μm/45 μm to 45 μm/45 μm, the negative segregation behavior becomes weaker, and its Se increases from −0.084 to −0.007. When the WC/316 L size ratio increases to 65 μm/45 μm, the powder behaves positive segregation with $Se_{max} = 0.017$. In comparison with spherical WC powder, polyhedral WC shape can significantly reduce the negative segregation behavior of the powder bed, and its Se decreases from −0.019 to −0.008.

3. The density difference of WC and 316 L powders in the composite powder bed leads to the difference in the energy of these two powders (the WC powder contains more energy and the 316 L powder has less energy) and the difference in the force (the force in gravity direction on WC powder is obviously larger than that of the 316 L powder), resulting in a big difference in the velocities between the two powders (the WC powder has a larger velocity in the gravity

direction than the 316 L powder), which eventually leads to the segregation behavior in the composite powder bed.

4. For WC/316 L composite powder with a fixed composition, the big composition gradient structure (i.e., the big composition difference) can be obtained if the following conditions are met: (1) spreading velocity = 0.025 m/s; (2) WC/316 L size ratio = 25 μm/45 μm; (3) roller as the spreader; (4) spherical WC powder.

Declaration of Competing Interest

The authors declared that there is no conflict of interest.

Appendix A. Appendix

Table A1
Equations utilized in the simulations [38,42].

Forces and torques		Symbols	Equations
Normal direction	Interaction force	$F_{ij,n}$	$F_{ij,\,n} = F^n_{c,\,ij} + F^n_{d,\,ij}$
	Contact force	$F^n_{c,\,ij}$	$F^n_{c,ij} = \dfrac{4E^*}{3R^*}r^3 - 4\sqrt{\pi r^3 \gamma E^*}$
	Damping force	$F^n_{d,\,ij}$	$F^n_{d,ij} = -\sqrt{\dfrac{20}{3}}\beta\left[E^* m^* (R^* \alpha^n)^{\frac{1}{2}}\right]^{\frac{1}{2}} u^n_{ij}$
Tangential direction	Interaction force	$F_{ij,s}$	$F_{ij,\,s} = F^s_{c,\,ij} + F^s_{d,\,ij}$
	Contact force	$F^s_{c,\,ij}$	$F^s_{c,ij} = -\min\left\{F_f, \left\|8G^*\sqrt{R^*\alpha^n}\,\alpha^s\right\|\right\}$
	Damping force	$F^s_{d,\,ij}$	$F^s_{d,ij} = \sqrt{\dfrac{80}{3}}\beta\left[G^* m^* (R^* \alpha^n)^{\frac{1}{2}}\right]^{\frac{1}{2}} u^s_{ij}$
Friction force		F_f	$F_f = \mu_s \|F^n_{c,\,ij}\|$
Friction torque		$T_{f,ij}$	$T_{f,\,ij} = R_i \times F^s_{c,\,ij}$
Rolling torque		$T_{r,ij}$	$T_{r,ij} = -\mu_r R_i F^n_{c,ij}\,\widehat{\omega_i}$

Note: in Table A1,

$R^* = R_i R_j/(R_i + R_j)$, $m^* = m_i m_j/(m_i + m_j)$, $E^* = E_i E_j/[E_i(1-\sigma_j^2) + E_j(1-\sigma_i^2)]$,

$G^* = G_i G_j/[G_i(1-\sigma_j) + G_j(1-\sigma_i)]$, $\widehat{\omega_i} = \omega_i/|\omega_i|$. R_i, m_i, E_i, G_i, σ_i and R_j, m_j E_j, G_j, σ_j are the radius, mass, Young's modulus, shear modulus and Poisson's ratio of particle i and particle j, respectively; γ, μ_s, μ_r are the surface energy, sliding and rolling friction coefficients; u^n_{ij} and u^s_{ij} are the normal and tangential relative velocities when a collision occurs between particles i and j; α^n and α^s are the normal and tangential overlaps when a collision occurs between particles i and j.
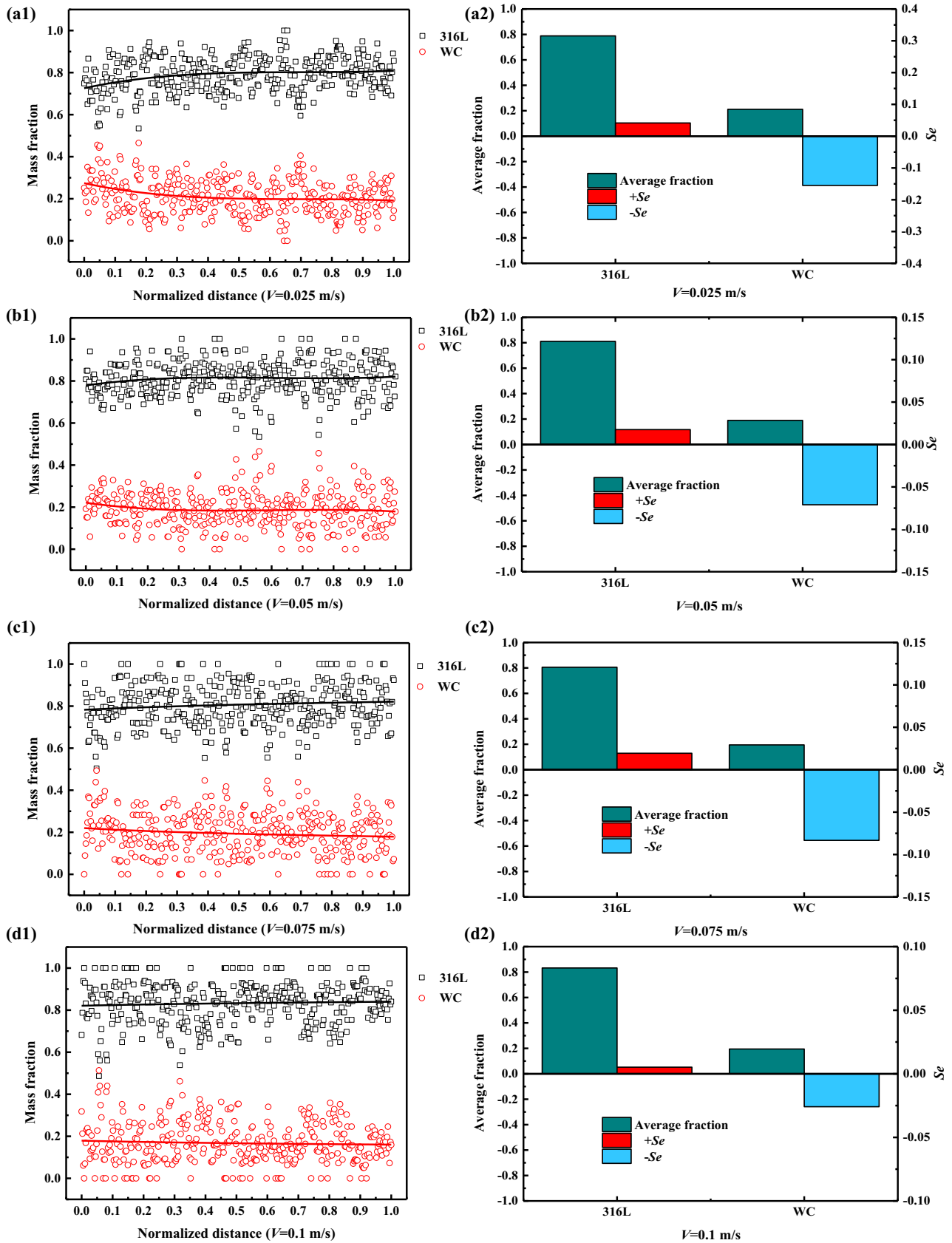
Fig. A1. (a) Mass fraction evolutions of each composition and (b) corresponding average fractions and segregation degrees under different blade velocities.
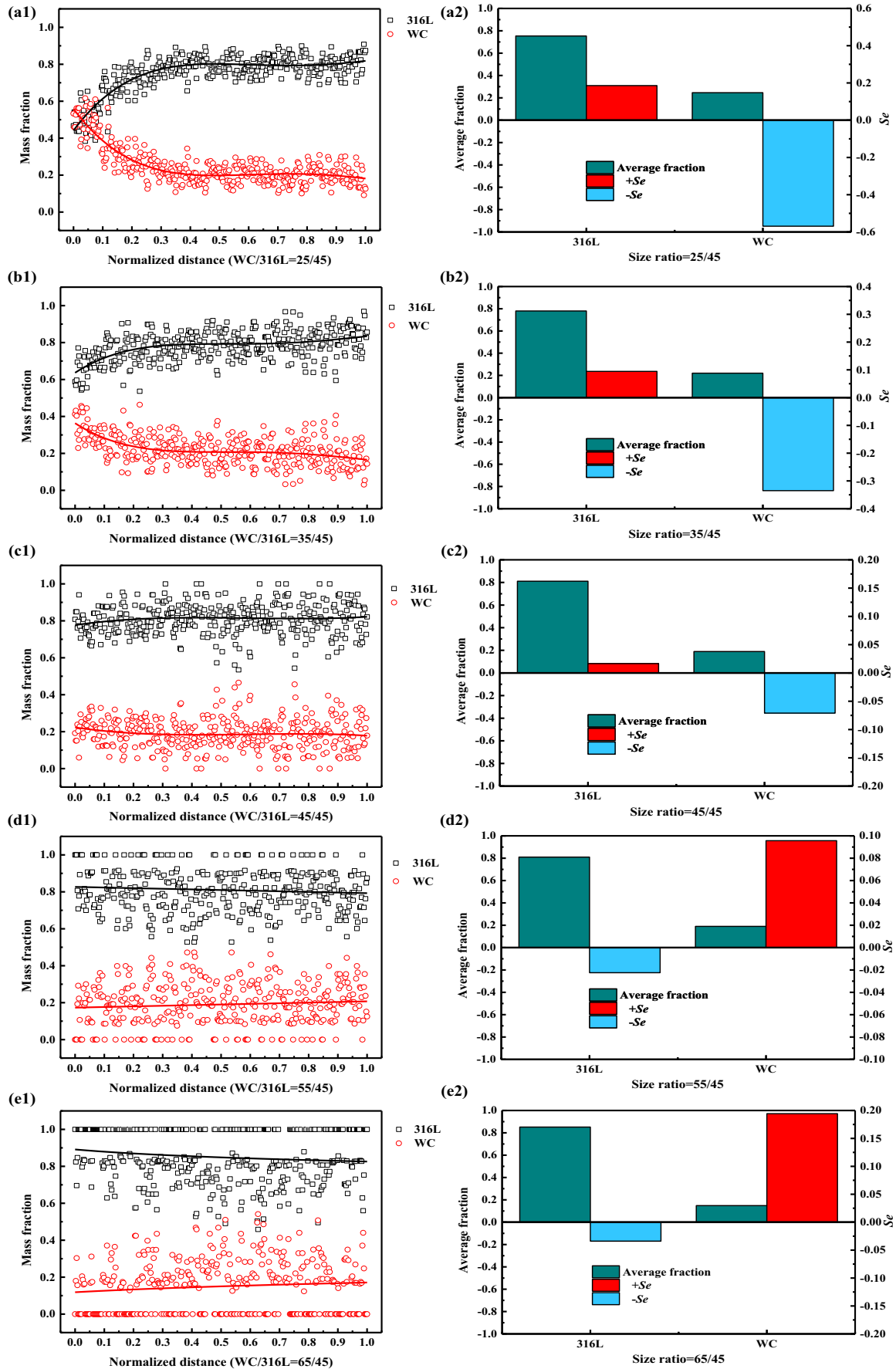
Fig. A2. (a) Mass fraction evolutions of each composition and (b) corresponding average fractions and segregation degrees under different WC/316 L size ratios.
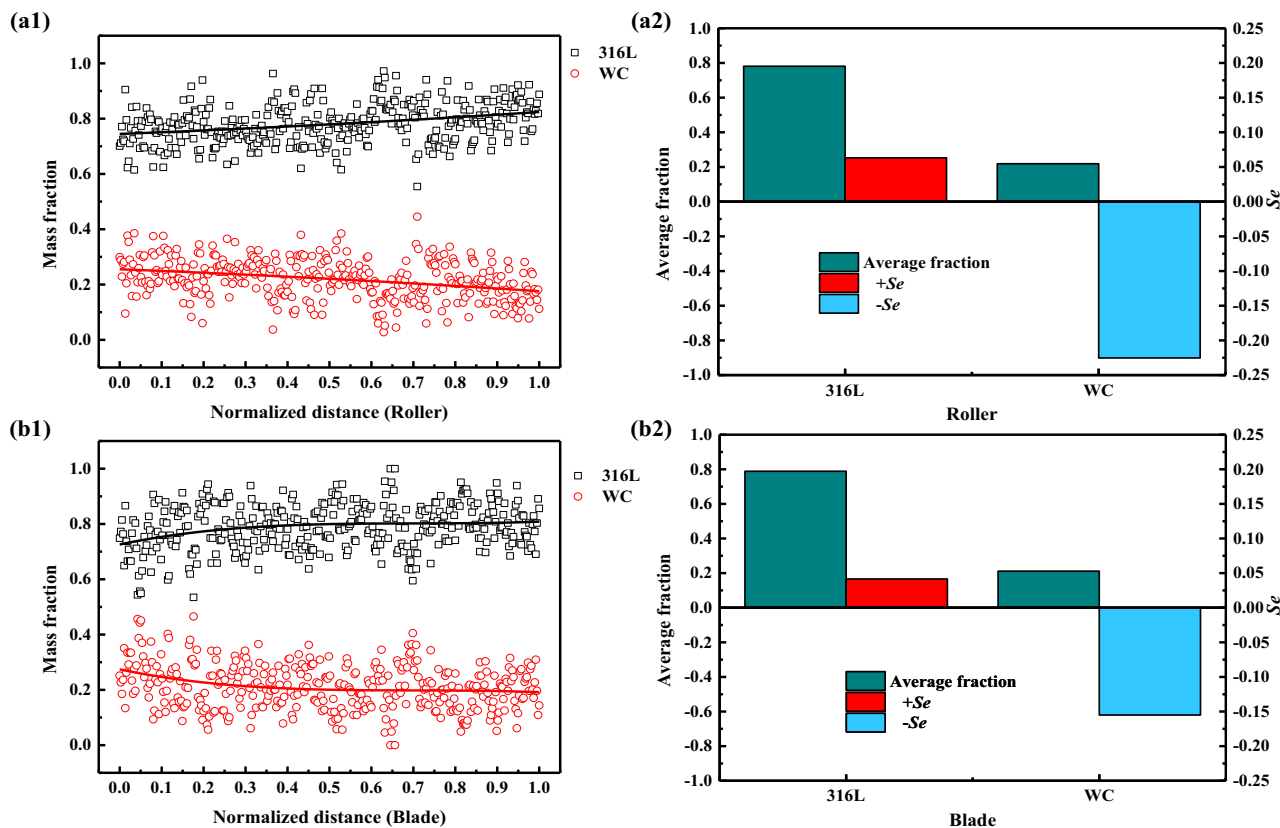
Fig. A3. (a) Mass fraction evolutions of each composition and (b) corresponding average fractions and segregation degrees under different spreader geometries.
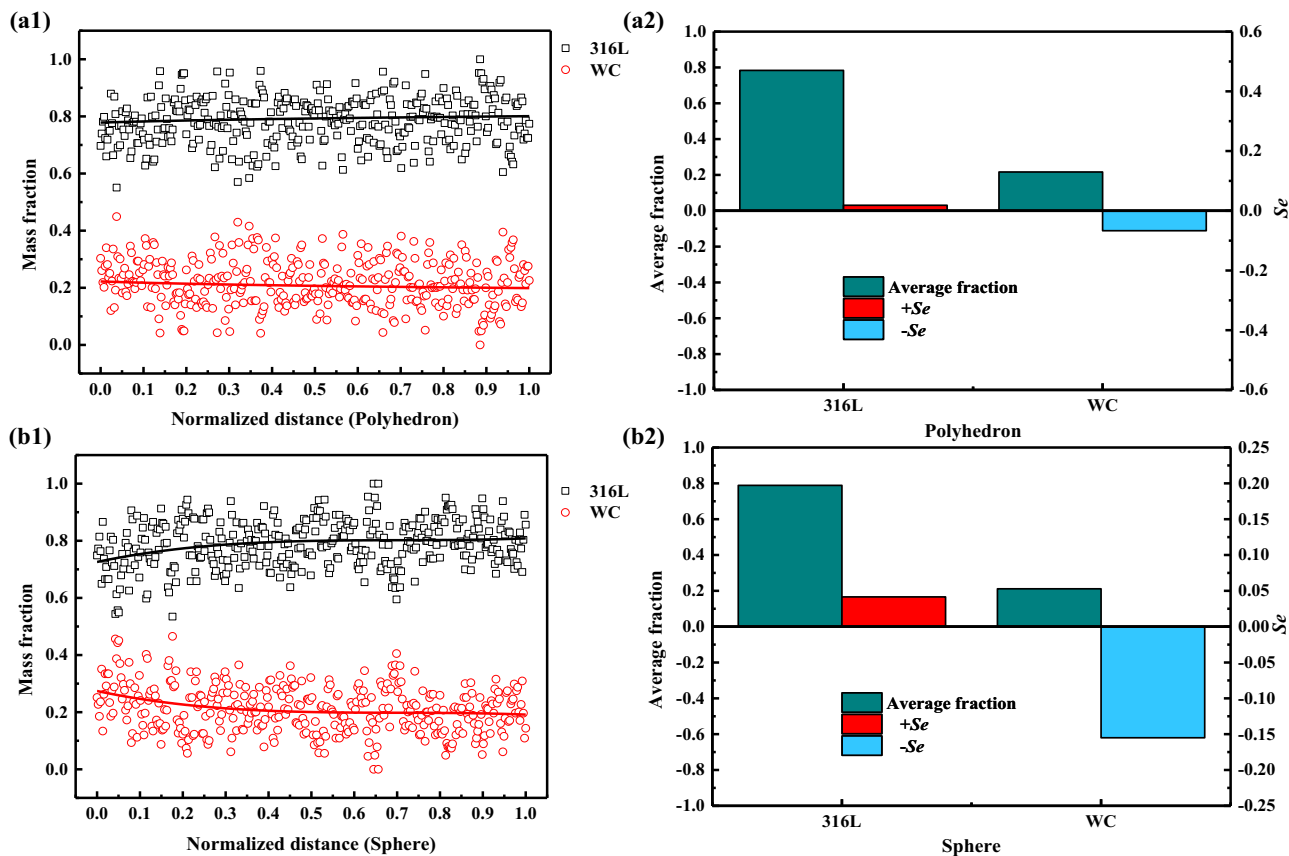

Fig. A4. (a) Mass fraction evolutions of each composition and (b) corresponding average fractions and segregation degrees under different WC shapes.

References

[1] L. Raimondi, L. Tomesani, L. Donati, A. Zucchelli, Lattice material infiltration for hybrid metal-composite joints: manufacturing and static strenght, Compos. Struct. 269 (2021), 114069.

[2] C.L. Tan, J. Zou, D. Wang, W.Y. Ma, K.S. Zhou, Duplex strengthening via SiC addition and in-situ precipitation in additively manufactured composite materials, Compos. Part B 236 (2022), 109820.

[3] R. Ekici, E. Kosedag, M. Demir, Repeated low-velocity impact responses of SiC particle reinforced Al metal-matrix composites, Ceram. Int. 48 (2022) 5338–5351.

[4] F. Saba, F.M. Zhang, S.L. Liu, T.F. Liu, Reinforcement size dependence of mechanical properties and strengthening mechanisms in diamond reinforced titanium metal matrix composites, Compos. Part B 167 (2019) 7–19.

[5] Y.J. Fang, M.-K. Kim, Y.L. Zhang, Z.Y. Duan, Q. Yuan, J. Suhr, Particulate-reinforced iron-based metal matrix composites fabricated by selective laser melting: a systematic review, J. Manuf. Process. 74 (2022) 592–639.

[6] H.Y. Chen, D.D. Gu, K. Kosiba, T.W. Lu, L. Deng, L.X. Xi, U. Kühn, Achieving high strength and high ductility in WC-reinforced iron-based composites by laser additive manufacturing, Addit. Manufact. 35 (2020), 101195.

[7] T. Anandaraj, P.P. Sethusundaram, C. Chanakyan, S. Sakthivelu, M. Meignanamoorthy, Influence of different reinforcements on properties of metal matrix composites: a review, Mater. Today Proc. 37 (2021) 3480–3484.

[8] N. Bharat, P.S.C. Bose, An overview on the effect of reinforcement and wear behaviour of metal matrix composites, Mater. Today Proc. 46 (2021) 707–713.

[9] K.G. Luo, H.Q. Xiong, Y. Zhang, H. Gu, Z.D. Li, C. Kong, H.L. Yu, AA1050 metal matrix composites reinforced by high-entropy alloy particles via stir casting and subsequent rolling, J. Alloys Compd. 893 (2022), 162370.

[10] U.R. Kanth, P.S. Rao, M.G. Krishna, Mechanical behaviour of fly ash/SiC particles reinforced Al-Zn alloy-based metal matrix composites fabricated by stir casting method, J. Mater. Res. Technol. 8 (2019) 737–744.

[11] P.K. Jain, P. Baredar, S.C. Soni, Microstructure and mechanical properties of silicon carbide particle reinforced aluminium 6101 metal matrix composite produced by two-step stir casting, Mater. Today Proc. 26 (2020) 2740–2745.

[12] G. Manohar, K.M. Pandey, S.R. Maity, Characterization of boron carbide (B4C) particle reinforced aluminium metal matrix composites fabricated by powder metallurgy techniques-a review, Mater. Today Proc. 45 (2021) 6882–6888.

[13] E.M. Parsons, S.Z. Shaik, Additive manufacturing of aluminum metal matrix composites: mechanical alloying of composite powders and single track consolidation with laser powder bed fusion, Addit. Manufact. 50 (2022), 102450.

[14] Y.M. Zhang, Y.F. Yu, L. Wang, Y. Li, F. Lin, W.T. Yan, Dispersion of reinforcing micro-particles in the powder bed fusion additive manufacturing of metal matrix composites, Acta Mater. 235 (2022), 118086.

[15] X.C. Yan, C.J. Huang, C.Y. Chen, R. Bolot, L. Dembinski, R.Z. Huang, W.Y. Ma, H.L. Liao, M. Liu, Additive manufacturing of WC reinforced maraging steel 300 composites by cold spraying and selective laser melting, Surf. Coat. Technol. 371 (2019) 161–171.

[16] D.D. Gu, J. Ma, H.Y. Chen, K.J. Lin, L.X. Xi, Laser additive manufactured WC reinforced Fe-based composites with gradient reinforcement/matrix interface and enhanced performance, Compos. Struct. 192 (2018) 387–396.

[17] J.Z. Lu, J. Cao, H.F. Lu, L.Y. Zhang, K.Y. Luo, Wear properties and microstructural analyses of Fe-based coatings with various WC contents on H13 die steel by laser cladding, Surf. Coat. Technol. 369 (2019) 228–237.

[18] Q. Xiao, W.L. Sun, K.X. Yang, X.F. Xing, Z.H. Chen, H.N. Zhou, J. Lu, Wear mechanisms and micro-evaluation on WC particles investigation of WC-Fe composite coatings fabricated by laser cladding, Surf. Coat. Technol. 420 (2021), 127341.

[19] Y.L. Xia, H.N. Chen, X.D. Liang, J.B. Lei, Circular oscillating laser melting deposition of nickel-based superalloy reinforced by WC: microstructure, wear resistance and electrochemical properties, J. Manuf. Process. 68 (2021) 1694–1704.

[20] L.D. Bobbio, B. Bocklund, Z.-K. Liu, A.M. Beese, Tensile behavior of stainless steel 304L to Ni-20Cr functionally graded material: experimental characterization and computational simulations, Materialia 18 (2021), 101151.

[21] S.L. Mao, D.Z. Zhang, Z.H. Ren, G. Fu, X.Y. Ma, Effects of process parameters on interfacial characterization and mechanical properties of 316L/CuCrZr functionally graded material by selective laser melting, J. Alloys Compd. 899 (2022), 163256.

[22] K. Zhao, G.H. Zhang, G.Y. Ma, C. Shen, D.J. Wu, Microstructure and mechanical properties of titanium alloy / zirconia functionally graded materials prepared by laser additive manufacturing, J. Manuf. Process. 56 (2020) 616–622.

[23] C.H. Zhang, H. Zhang, C.L. Wu, S. Zhang, Z.L. Sun, S.Y. Dong, Multi-layer functional graded stainless steel fabricated by laser melting deposition, Vacuum 141 (2017) 181–187.

[24] Y. Zhang, A. Bandyopadhyay, Direct fabrication of compositionally graded Ti-Al2O3 multi-material structures using laser engineered net shaping, Addit. Manufact. 21 (2018) 104–111.

[25] Y. Zhang, A. Bandyopadhyay, Direct fabrication of bimetallic Ti6Al4V+Al12Si structures via additive manufacturing, Addit. Manufact. 29 (2019), 100783.

[26] S.Y. Zhang, L.L. Wang, X. Lin, H.O. Yang, W.D. Huang, The formation and dissolution mechanisms of laves phase in Inconel 718 fabricated by selective laser melting compared to directed energy deposition and cast, Compos. Part B 239 (2022), 109994.

[27] M. Godec, S. Malej, D. Feizpour, Č. Donik, M. Balažic, D. Klobčar, L. Pambaguian, M. Conradi, A. Kocijan, Hybrid additive manufacturing of Inconel 718 for future space applications, Mater. Charact. 172 (2021), 110842.

[28] H.L. Wei, Y. Cao, W.H. Liao, T.T. Liu, Mechanisms on inter-track void formation and phase transformation during laser powder bed fusion of Ti-6Al-4V, Addit. Manufact. 34 (2020), 101221.

[29] N.S. Al-Mamun, K. Mairaj Deen, W. Haider, E. Asselin, I. Shabib, Corrosion behavior and biocompatibility of additively manufactured 316L stainless steel in a physiological environment: the effect of citrate ions, Addit. Manufact. 34 (2020), 101237.

[30] S. Waqar, K. Guo, J. Sun, Evolution of residual stress behavior in selective laser melting (SLM) of 316L stainless steel through preheating and in-situ re-scanning techniques, Opt. Laser Technol. 149 (2022), 107806.

[31] Y. He, A. Hassanpour, A.E. Bayly, Linking particle properties to layer characteristics: discrete element modelling of cohesive fine powder spreading in additive manufacturing, Addit. Manufact. 36 (2020), 101685.

[32] H. Chen, Y.X. Chen, Y. Liu, Q.S. Wei, Y.S. Shi, W.T. Yan, Packing quality of powder layer during counter-rolling-type powder spreading process in additive manufacturing, Int. J. Mach. Tools Manuf. 153 (2020), 103553.

[33] D.Z. Yao, J. Wang, M. Li, T.T. Zhao, Y. Cai, X.Z. An, R.P. Zou, H. Zhang, H.T. Fu, X. H. Yang, Q.C. Zou, Segregation of 316L stainless steel powder during spreading in selective laser melting based additive manufacturing, Powder Technol. 397 (2022), 117096.

[34] A. Mussatto, R. Groarke, A. O'Neill, M.A. Obeidi, Y. Delaure, D. Brabazon, Influences of powder morphology and spreading parameters on the powder bed topography uniformity in powder bed fusion metal additive manufacturing, Addit. Manufact. 38 (2021), 101807.

[35] J.T. Zhang, Y.Q. Tan, X.W. Xiao, S.Q. Jiang, Comparison of roller-spreading and blade-spreading processes in powder-bed additive manufacturing by DEM simulations, Particuology 66 (2022) 48–58.

[36] L. Wang, E.L. Li, H.P. Shen, R.P. Zou, A.B. Yu, Z.Y. Zhou, Adhesion effects on spreading of metal powders in selective laser melting, Powder Technol. 363 (2020) 602–610.

[37] M.M.H.D. Arntz, H.H. Beeftink, W.K. den Otter, W.J. Briels, R.M. Boom, Segregation of granular particles by mass, radius, and density in a horizontal rotating drum, AICHE J. 60 (2014) 50–59.

[38] D.Z. Yao, X.Z. An, H.T. Fu, H. Zhang, X.H. Yang, Q.C. Zou, K.J. Dong, Dynamic investigation on the powder spreading during selective laser melting additive manufacturing, Addit. Manufact. 37 (2021), 101707.

[39] Q. Wu, C. Qiao, J. Wang, D.Z. Yao, Y.H. Wu, W. Fan, M. Li, X.Z. An, Adaptability investigations on bottom modified blade in powder spreading process of additive manufacturing, Addit. Manufact. 49 (2021), 102477.

[40] W.G. Nan, M. Pasha, M. Ghadiri, Effect of gas-particle interaction on roller spreading process in additive manufacturing, Powder Technol. 372 (2020) 466–476.

[41] J. Wang, D.Z. Yao, M. Li, X.Z. An, S.J. Li, W.T. Hou, X. Zhang, G.Y. Yang, J. Wang, L. Wang, Hierarchical effects of multi-layer powder spreading in the electron beam powder bed fusion additive manufacturing of pure tungsten material, Addit. Manufact. 55 (2022), 102835.

[42] H. Chen, Q.S. Wei, S.F. Wen, Z.W. Li, Y.S. Shi, Flow behavior of powder particles in layering process of selective laser melting: numerical modeling and experimental verification based on discrete element method, Int. J. Mach. Tools Manuf. 123 (2017) 146–159.

[43] D.Z. Yao, X.H. Liu, J. Wang, W. Fan, M. Li, H.T. Fu, H. Zhang, X.H. Yang, Q.C. Zou, X.Z. An, Numerical insights on the spreading of practical 316 L stainless steel powder in SLM additive manufacturing, Powder Technol. 390 (2021) 197–208.

[44] Z.J. Zuo, S.G. Gong, G.L. Xie, J.P. Zhang, DEM simulation of binary mixing particles with different density in an intensive mixer, Powder Technol. 383 (2021) 454–470.

[45] H.C. Li, Y.B. Hu, R.F. Di, R.W. Yuan, C. Shi, J.B. Lei, Effects of WC particles on microstructure and mechanical properties of 316L steel obtained by laser melting deposition, Ceram. Int. 48 (2022) 20388–20399.

[46] Z.H. Li, B.R. Teng, B.B. Yao, J. Liu, Microstructure and mechanical properties of WC reinforced 18Ni300 composites produced by selective laser melting, Mater. Charact. 180 (2021), 111406.

[47] C.-W. Li, K.-C. Chang, A.-C. Yeh, On the microstructure and properties of an advanced cemented carbide system processed by selective laser melting, J. Alloys Compd. 782 (2019) 440–450.

[48] H. Chen, T. Cheng, Z.W. Li, Q.S. Wei, W.T. Yan, Is high-speed powder spreading really unfavourable for the part quality of laser powder bed fusion additive manufacturing? Acta Mater. 231 (2022), 117901.

[49] W.G. Nan, M. Pasha, M. Ghadiri, Numerical simulation of particle flow and segregation during roller spreading process in additive manufacturing, Powder Technol. 364 (2020) 811–821.

[50] M.Y. Shaheen, A.R. Thornton, S. Luding, T. Weinhart, The influence of material and process parameters on powder spreading in additive manufacturing, Powder Technol. 383 (2021) 564–583.

[51] H. Chen, Q. Wei, Y. Zhang, F. Chen, Y. Shi, W. Yan, Powder-spreading mechanisms in powder-bed-based additive manufacturing: experiments and computational modeling, Acta Mater. 179 (2019) 158–171.

[52] L.J. Mao, M.J. Cai, Q.Y. Liu, L.F. Han, Effects of spherical WC powders on the erosion behavior of WC-Ni hardfacing used for steel body drill bit, Surf. Coat. Technol. 409 (2021) 126893.

[53] Y.L. Wu, X.Z. An, A.B. Yu, DEM simulation of cubical particle packing under mechanical vibration, Powder Technol. 314 (2017) 89–101.

[54] B. Zhao, X.Z. An, H. Zhao, L.L. Shen, X.D. Sun, Z.Y. Zhou, DEM simulation of the local ordering of tetrahedral granular matter, Soft Matter 15 (2019) 2260–2268.

[55] L. Wang, A.B. Yu, E.L. Li, H.P. Shen, Z.Y. Zhou, Effects of spreader geometry on powder spreading process in powder bed additive manufacturing, Powder Technol. 384 (2021) 211–222.

[56] H.Y. Zhao, X.Z. An, K.J. Dong, R.Y. Yang, F. Xu, H.T. Fu, H. Zhang, X.H. Yang, Macro- and microscopic analyses of piles formed by platonic solids, Chem. Eng. Sci. 205 (2019) 391–400.